3D angle gathers from wave-equation extended images

Tongning Yang and Paul Sava, Center for Wave Phenomena, Colorado School of Mines*

SUMMARY

We present a method to construct 3D angle gathers from extended images obtained using wave-equation migration. The method relies on an analytic formula that associates the reflection and azimuth angle to reflection kinematics in the images. The decomposition is able to render the angle gathers that characterize the reflectivity as a function of both reflection and azimuth angle simultaneously. Since the images are constructed from accurate wave-equation-based imaging algorithm, the method is robust to characterize angle information in presence of noisy data and complex subsurface geologic environments. The application of the method on a North Sea 3D OBC field dataset illustrates that 3D angle gathers obtained from our method is effective to extract reflection and azimuth angle information.

INTRODUCTION

Characterizing the subsurface structure is one of the most important tasks for seismic imaging. Wave-equation-based imaging algorithms such as downward continuation or reverse-time migration are powerful tools to image the subsurface in complex geologic environments (Gray et al., 2001). Nonetheless, a structural description of the subsurface alone is not sufficient for oil and gas exploration. It is always necessary to construct images expressing reflectivity as a function of reflection angles. Such images are commonly known as angle gathers, and they can be used for subsurface illumination analysis, velocity model accuracy evaluation, and amplitude-verse angle analysis.

Angle gathers can be produced using either ray methods (Xu et al., 1998; Brandsberg-Dahl et al., 2003) or by using wavefield methods (de Bruin et al., 1990; Mosher et al., 1997; Prucha et al., 1999; Xie and Wu, 2002; Rickett and Sava, 2002; Sava and Fomel, 2003; Biondi and Symes, 2004; Wu and Chen, 2006). The resulting gathers share similar characteristics since they simply describe the reflectivity as a function of incidence angles at the reflected interface. When using wavefield methods, angle decomposition can be implemented either before or after the application of an imaging condition. The two classes of methods differ by the input used to characterize the angle-dependent illumination of subsurface geology. The methods operating before the imaging condition decompose the extrapolated wavefields from the source and receivers (de Bruin et al., 1990; Mosher et al., 1997; Prucha et al., 1999; Wu and Chen, 2006). Angle decomposition can also be done after the imaging condition. This kind of method decomposes the images themselves which are represented as a function of space and additional parameters, typically refered to as *extensions* (Rickett and Sava, 2002; Sava and Fomel, 2003, 2006; Sava and Vasconcelos, 2011).

In this article, we develop a methodology for constructing angle gathers in 3D using extended images. In particular, we use space-lag extended images to produce reflection and azimuth angle gathers simultaneously. The angle decomposition is based on an analytic formula that characterizes the reflection kinematics in the space-lag gathers. We use both a synthetic and North Sea 3D OBC field dataset to demonstrate our method.

THEORY

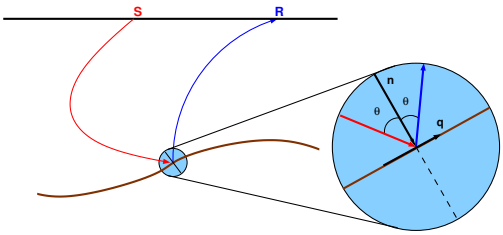

Figure 1: Cartoon describing wave propagation in an inhomogeneous medium. The wavepaths in the local region around the reflection point can be approximated with straight lines.

The popular wave-equation migration procedure consists of two main steps: wavefield reconstruction and imaging condition. An imaging condition extracts the locations where reflections occur in the subsurface from reconstructed wavefields:

$$R\left(\mathbf{x}\right) = \sum_t W_s\left(\mathbf{x},t\right) W_r\left(\mathbf{x},t\right) \ . \tag{1}$$

W_s and W_r stand for the source and receiver wavefields, respectively. An alternative extended imaging condition (Rickett and Sava, 2002; Sava and Fomel, 2006) generalizes the conventional imaging condition by preserving non-zero cross-correlation lags in the output image:

$$R\left(\mathbf{x},\boldsymbol{\lambda},\tau\right) = \sum_t W_s\left(\mathbf{x}-\boldsymbol{\lambda},t-\tau\right) W_r\left(\mathbf{x}+\boldsymbol{\lambda},t+\tau\right) . \tag{2}$$

The quantities $\boldsymbol{\lambda}$ and τ are the cross-correlation lags applied to the source and receiver wavefields in spatial and temporal directions.

To apply angle decomposition to space-lag extended images, one has to derive the formula describing the reflection kinematics in the images. The derivation follows the idea developed in (Yang and Sava, 2010). Assuming plane-wave propagation, the source and receiver plane-waves are described by:

$$\mathbf{p}_s \cdot \mathbf{x} \ = \ Vt \ , \tag{3}$$

$$\mathbf{p}_r \cdot \left(\mathbf{x} - 2d\mathbf{n}\right) \ = \ Vt \ , \tag{4}$$

where $\mathbf{p}_s$ and $\mathbf{p}_r$ are the slowness vector of the source and receiver plane-waves, respectively, $d\mathbf{n}$ characterizes the position of the reflection point, $\mathbf{n}$ is the unit vectors normal to the reflection plane, and V is the local velocity. We can also obtain

the shifted source and receiver plane-waves by introducing the space-lags

$$\mathbf{p}_s \cdot (\mathbf{x} + \boldsymbol{\lambda}) = Vt \,, \quad (5)$$

$$\mathbf{p}_r \cdot (\mathbf{x} - 2d\mathbf{n} - \boldsymbol{\lambda}) = Vt \,. \quad (6)$$

We have the following relations for the reflection geometry as shown in Figure 1:

$$\mathbf{p}_s - \mathbf{p}_r = 2\mathbf{n}\cos\theta \,, \quad (7)$$

$$\mathbf{p}_s + \mathbf{p}_r = 2\mathbf{q}\sin\theta \,, \quad (8)$$

where $\mathbf{q}$ is unit vector parallel to the reflection plane, and θ is the reflection angle. The azimuth angle ϕ is embedded in $\mathbf{q}$. We can combine the system of equations 5-6 and obtain the moveout function as follows:

$$z(\boldsymbol{\lambda}) = z_0 - \frac{\tan\theta\,(\mathbf{q}\cdot\boldsymbol{\lambda})}{n_z} \,. \quad (9)$$

In the equation above, z_0 is simply the location of the image point at zero space lag, and n_z is the vertical component of $\mathbf{n}$. For the angle decomposition formula above, the following equation is combined to eliminate the dependency on λ_z:

$$\mathbf{n}\cdot\boldsymbol{\lambda} = 0 \,. \quad (10)$$

In practice, we only need to compute the space-lag extension along the inline and crossline directions. λ_z can be expressed in terms of λ_x and λ_y via equation 10. Then we apply equation 9 for angle decomposition to space-lag gathers.

Alternatively, one can also apply angle decomposition to common-image-point gathers, using the the formula in (Sava and Vlad, 2011):

$$(\mathbf{q}\cdot\boldsymbol{\lambda})\sin\theta = V\tau \,, \quad (11)$$

EXAMPLES

In this section, we first demonstrate our method using a synthetic model, and then we show the application of the method to a North Sea 3D field dataset.

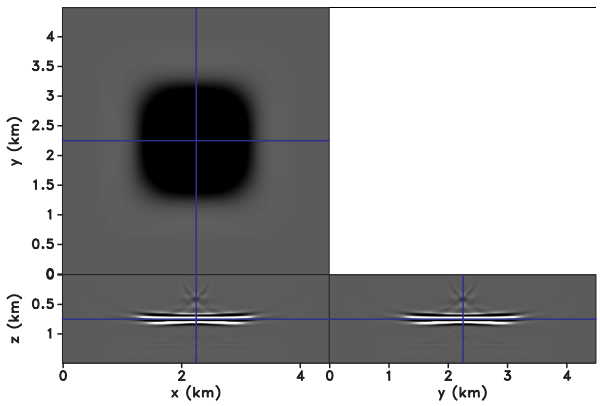

Figure 2: The migrated image of a synthetic one flat interface, constant velocity model.

Figure 2 shows the image obtained for the synthetic model, which has constant velocity with one flat interface located at $Z = 0.75$ km. The image corresponds to the shot at the center of the model. We conduct two sets of experiments to test our algorithm. The first set of experiments constructs the space-lag gathers such that they correspond to the same reflection angle but different azimuth angle. The four locations are $(2.7, 2.25)$ km, $(2.25, 2.7)$ km, $(1.8, 2.25)$ km, and $(2.25, 1.8)$ km, respectively. Figure 3(a)-3(d) show the space-lag gathers at these locations. As the model contains only one reflector, we slice the angle gathers at the depth of interface to highlight the angle distribution, as shown in Figure 3(e)-3(h). The second set of experiment constructs the space-lag gathers such that they correspond to the same azimuth angle but different reflection angle. The four locations are $(1.8, 1.8)$ km, $(2.25, 2.25)$ km, $(2.7, 2.7)$ km, and $(3.15, 3.15)$ km, respectively. Figure 4(a)-4(d) show the space-lag gathers at these locations, and the depth slices of the corresponding angle gathers are plotted in Figure 4(e)-4(h). In both cases, we see that our angle decomposition method accurately captures the reflection and azimuth angle information.

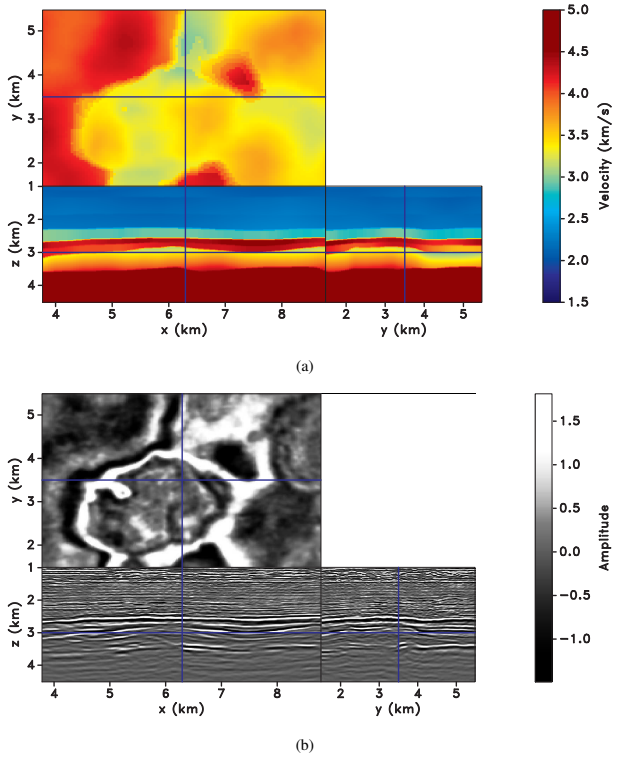

Figure 5: North Sea field data example. (a) The velocity model and (b) the corresponding migrated image.

We also apply our method to a North Sea 3D OBC field dataset. The data are acquired in the Volve field Szydlik et al. (2007). Figure 5(a) shows the velocity model, and Figure 5(b) plots the corresponding migrated image. We follow the same workflow to construct the 3D angle gathers at $(6.35, 3.45)$ km. The input space-lag gathers are shown in Figure 6(a), and the angle decomposition result is plotted in Figure 6(b). From the angle gathers, we are able to analyze the subsurface illumination distribution and velocity model accuracy as well. In this case, we see that the event around $Z = 2.64$ km in reflection

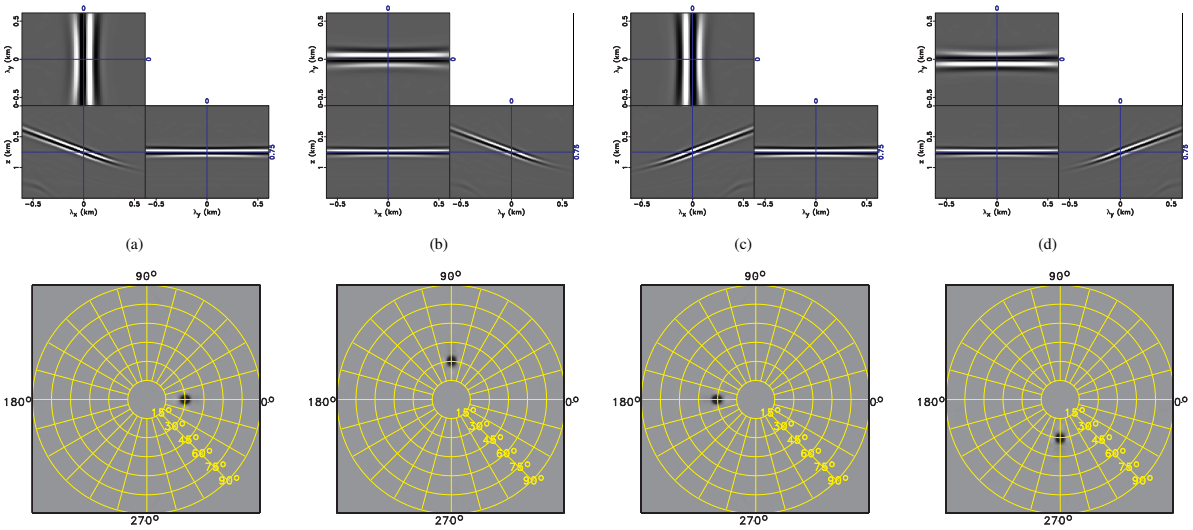

Figure 3: The space-lag gathers at locations corresponding to (a) $\theta = 30^\circ$, $\phi = 0^\circ$, (b) $\theta = 30^\circ$, $\phi = 90^\circ$, (c) $\theta = 30^\circ$, $\phi = 180^\circ$, and (d) $\theta = 30^\circ$, $\phi = 270^\circ$. The 3D angle gathers from space-lag gathers sliced at the depth of interface corresponding to (e) $\theta = 30^\circ$, $\phi = 0^\circ$, (f) $\theta = 30^\circ$, $\phi = 90^\circ$, (g) $\theta = 30^\circ$, $\phi = 180^\circ$, and (h) $\theta = 30^\circ$, $\phi = 270^\circ$.

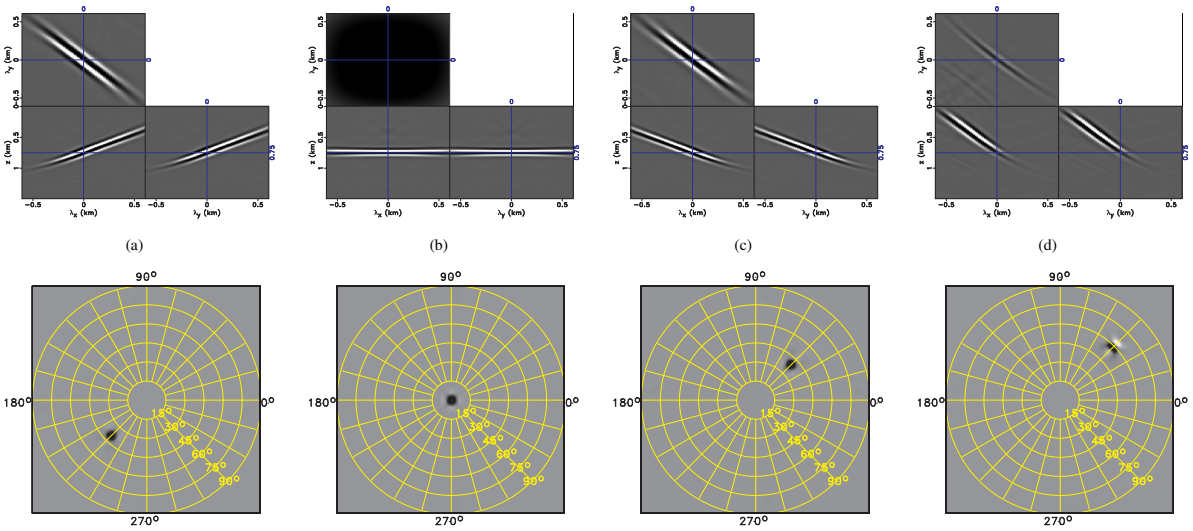

Figure 4: The space-lag gathers at locations corresponding to (a) $\theta = 38^\circ$, $\phi = 225^\circ$, (b) $\theta = 0^\circ$, $\phi = 0^\circ$, (c) $\theta = 38^\circ$, $\phi = 45^\circ$, and (d) $\theta = 60^\circ$, $\phi = 45^\circ$. The 3D angle gathers from space-lag gathers sliced at the depth of interface corresponding to (e) $\theta = 38^\circ$, $\phi = 225^\circ$, (f) $\theta = 0^\circ$, $\phi = 0^\circ$, (g) $\theta = 38^\circ$, $\phi = 45^\circ$, and (h) $\theta = 60^\circ$, $\phi = 45^\circ$.

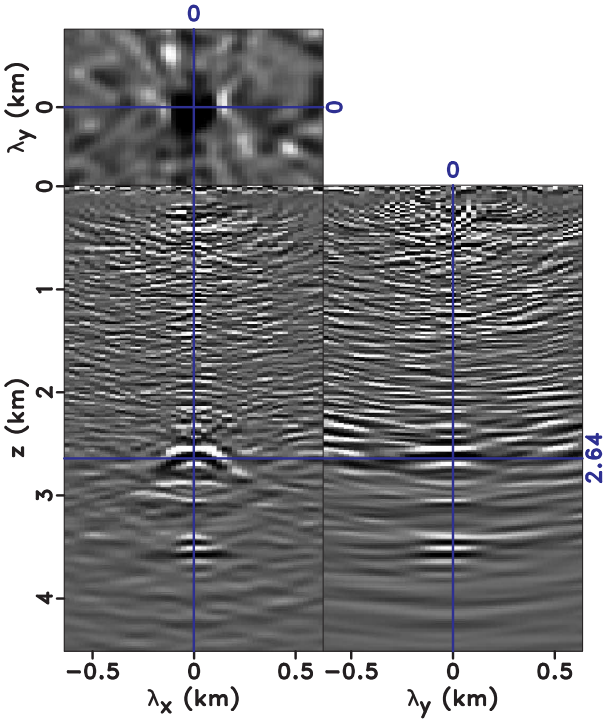

(a)

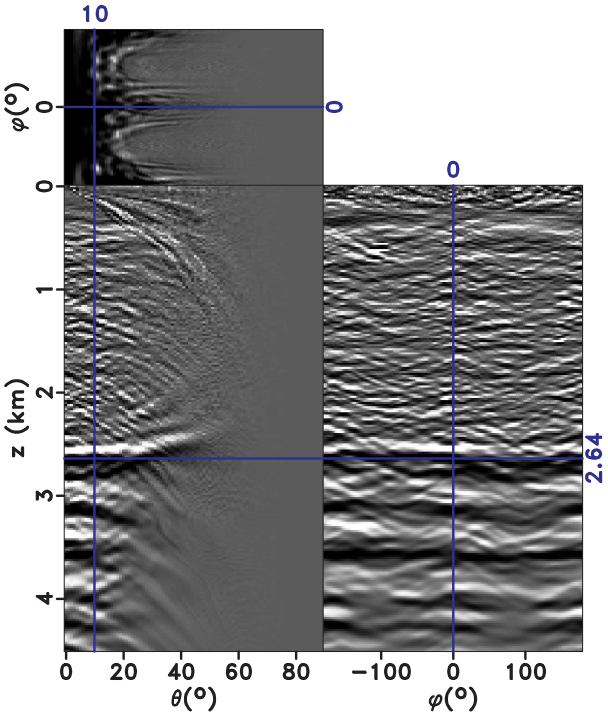

(b)

Figure 6: (a) 3D space-lag gathers at $X = 6.35$ km $Y = 3.45$ km. (b) 3D angle gathers obtained from Figure 6(a) using our method.

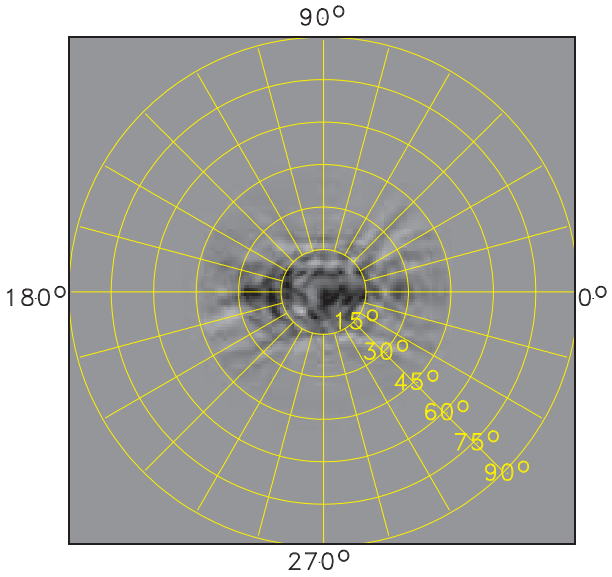

Figure 7: Depth slice of the angle gathers in Figure 6(b) at $Z = 2.64$ km.

angle panel shows residual moveout, which might be an indication of the velocity model error. In addition, the reflection angle illumination is limited to small angles (less than 40°, while the azimuth angle is mainly illuminated along the inline direction (0° and 180°). To obtain a better visualization of the angle distribution, we extract the slide at $Z = 2.64$ km from the angle gathers and plot it in polar coordinates as shown in Figure 7. The plot clearly shows that the subsurface is mainly illuminated along the inline direction.

CONCLUSIONS

We develop a 3D angle-decomposition method applied to space-lag extended images. The method extracts the reflection and azimuth angle information from the reflection moveout using the kinematics function related to the angles. The synthetic example validates the accuracy of the method to characterize the angle information. The North Sea field data example demonstrates that our method can be a useful tool for analyzing the velocity model accuracy and azimuthal illumination distribution.

ACKNOWLEDGMENTS

We thank sponsor companies of the Consortium Project on Seismic Inverse Methods for Complex Structures, whose support made this research possible. The authors would also like to thank Statoil ASA and the Volve license partners ExxonMobil E&P Norway and Bayerngas Norge, for the release of the Volve data.

REFERENCES

Biondi, B., and W. Symes, 2004, Angle-domain common-image gathers for migration velocity analysis by wavefield-continuation imaging: Geophysics, **69**, 1283–1298.

Brandsberg-Dahl, S., M. V. de Hoop, and B. Ursin, 2003, Focusing in dip and AvA compensation on scattering-angle/azimuth common image gathers: Geophysics, **68**, 232–254.

de Bruin, C. G. M., C. P. A. Wapenaar, and A. J. Berkhout, 1990, Angle-dependent reflectivity by means of prestack migration: Geophysics, **55**, 1223–1234.

Gray, S. H., J. Etgen, J. Dellinger, and D. Whitmore, 2001, Seismic migration problems and solutions: Geophysics, **66**, 1622–1640.

Mosher, C. C., D. J. Foster, and S. Hassanzadeh, 1997, Common angle imaging with offset plane waves: 67th Ann. Internat. Mtg, Soc. of Expl. Geophys., 1379–1382.

Prucha, M., B. Biondi, and W. Symes, 1999, Angle-domain common image gathers by wave-equation migration: 69th Ann. Internat. Mtg, Soc. of Expl. Geophys., 824–827.

Rickett, J., and P. Sava, 2002, Offset and angle-domain common image-point gathers for shot-profile migration: Geophysics, **67**, 883–889.

Sava, P., and S. Fomel, 2003, Angle-domain common image gathers by wavefield continuation methods: Geophysics, **68**, 1065–1074.

———, 2006, Time-shift imaging condition in seismic migration: Geophysics, **71**, S209–S217.

Sava, P., and I. Vasconcelos, 2011, Extended imaging condition for wave-equation migration: Geophysical Prospecting, **59**, 35–55.

Sava, P., and I. Vlad, 2011, Wide-azimuth angle gathers for wave-equation migration: Geophysics, **76**, S131–S141.

Szydlik, T., P. Smith, S. Way, L. Aamodt, and C. Friedrich, 2007, 3d pp/ps prestack depth migration on the volve field: First break, **25**, 43–47.

Wu, R.-S., and L. Chen, 2006, Directional illumination analysis using beamlet decomposition and propagation: Geophysics, **71**, S147–S159.

Xie, X., and R. Wu, 2002, Extracting angle domain information from migrated wavefield: 72nd Ann. Internat. Mtg, Soc. of Expl. Geophys., 1360–1363.

Xu, S., H. Chauris, G. Lambare, and M. S. Noble, 1998, Common angle image gather: A new strategy for imaging complex media: 68th Ann. Internat. Mtg, Soc. of Expl. Geophys., 1538–1541.

Yang, T., and P. Sava, 2010, Moveout analysis of wave-equation extended images: Geophysics, **75**, S151–S161.